Co/N nanoparticles obtained from ZIF-67 supported on a C_3N_4/Polydopamine framework as a bifunctional electrocatalyst for rechargeable zinc-air batteries with high specific capacity

Beatriz J. Ferraz* [a,b], Junhua Kong [b], Bing Li [b], Christopher Blackman [a] and Liu Zhaolin[b]*

[a] Department of Chemistry
University College London
20 Gordon Street
London, WC1H 0AJ, UK

[b] Institute Institute of Materials Research and Engineering, Agency for Science, Technology, and Research (A*STAR),
Fusionopolis Way, Innovis, #08-03,
Singapore, 138634, Singapore

ABSTRACT

Metal N-doped carbons (M-N-C) and specifically cobalt-based N-doped carbons (Co-N-C) have attracted extensive attention as suitable multifunctional catalysts. Their high catalytic activity, originating from the strong coupling effect of Co with N, lead to the formation of active sites with suitable binding energies for promoting the discharging and charging reactions. Herein, we propose the synthesis of an efficient bifunctional electrocatalyst (ZIFCNDA) prepared by the introduction of Co ions during the polymerisation of dopamine, which lead to the direct doping of a carbon framework and the localized growth of Co-based MOFs polyhedrons, generating Co-based nanoparticles (Co NPs) upon pyrolysis. The C_3N_4-controlled polydopamine growth formed thin graphitized carbon nanosheets which can facilitate the transfer of electrons to the catalytically active sites. The ZIFCNDA catalyst was able to efficiently catalyse both the oxygen reduction (ORR) and oxygen evolution (OER) reactions). The ZAB containing the developed catalyst presented a long-term discharge of 600 h (at 5 mA cm^{-2}) and a high specific capacity of 686 mAh g^{-1}. The cell was able to cycle at a high current densities of 10 and 15 mA cm^{-2} for over 150h and 65h, respectively.

INTRODUCTION

The current increased demand for energy storage and conversion systems have been driving the development of more sustainable options such as metal-air batteries and fuel cells. In metal-air battery systems the oxygen reduction reaction and oxygen evolution reaction are essential for driving the discharging and charging processes, respectively, however low onset and half-wave potentials of ORR and high overpotentials of OER greatly reduces the reaction kinetics.[1–5] Consequently, efficient electrocatalysts are necessary to help drive these reactions by reducing the energy barrier and improving the overall activity but the currently commercially available Pt/C (ORR) and Ir/C (OER) electrocatalysts raise concerns regarding their scarcity, high cost and poor long-term stability.[6–8] Considering these drawbacks, bifunctional ORR/OER electrocatalysts have been thoroughly researched.[3] For instance, heteroatom doped carbon-

based materials have been considered promising electrocatalysts due to their large surface area, tunable structure, appropriate pore size, excellent conductivity, long-term stability and availability of source materials.[9,10] Nitrogen-doping can create abundant defects on the carbon framework, inducing a positive charge on adjacent carbon atoms which can promote the ORR; this charge localization may promote the favourable side-on adsorption of O_2 on the catalyst surface, weakening the O-O bond and therefore facilitating the transfer of electrons between the surface and dioxygen.[11,12] Furthermore, metal N-doped carbons (M-N-C), specifically cobalt-based N-doped carbons (Co-N-C) have attracted extensive attention as suitable multifunctional catalysts.[13–18] Their high catalytic activity, originating from the strong coupling effect of Co with N, leads to the formation of active sites with suitable binding energies for promoting the discharging and charging reactions.[6] Cobalt may also promote the catalytic graphitization of amorphous carbon,[17,19,20] however it has been challenging to prepare catalysts with relatively well dispersed cobalt-based nanoparticles on the graphitic carbon network, which is essential to promote even transport of electrons to the Co-based active sites and hence rate of reaction across the catalyst framework. Zeolitic imidazolate frameworks (ZIF), a type of metal organic frameworks (MOFs), are tetrahedral structures containing transition metal (TM) cations directly coordinated to N-rich sites via the imidazole linkers.[21,22] These structures have been studied as precursors for the formation of M-N-C catalysts due to their tunable and porous scaffold with a large surface area.[14,16,18,23,24] Nevertheless, upon pyrolysis, the porous nanostructure tends to collapse because of the aggregation of metal atoms into larger undesirable particles, volatility of N and the formation of random structures , which greatly reduces surface area, porosity and further reduces its catalytic activity.[6,16,25,26]

In this work, we developed a strategy to promote the formation of well distributed cobalt active sites, achieved due to the insertion of cobalt ions during the polymerization process of dopamine, instead of on a previously prepared framework (e.g. graphene, etc).[27] The Co ions were chelated by the N-~~atoms~~ ions on the dopamine precursor, immobilizing them on the carbon support. Following this, the addition of the 2-methylimidazole ligand led to the formation of Co-based ZIF (i.e. ZIF-67) particles, which upon pyrolysis at 900°C under N_2 atmosphere, originated well dispersed cobalt nanoparticles surrounded by a graphitized carbon shell on a layered graphitic carbon framework. This strategy not only avoided the excessive growth and aggregation of metal nanoparticles but also led to the controlled formation of a thin layered structure due to the addition of a C_3N_4 template during polydopamine synthesis. The catalysts' stable network provides different catalysis paths for a more efficient performance. Furthermore, this avoided the undesired formation of random and irregular structures or bulky spheres, which can lead to the reduction of the catalytically active surface area. This work explores a novel and simplified synthesis process for the formation of well-dispersed Co NPs on a graphitized N-doped carbon framework.

EXPERIMENTAL SECTION

Chemicals and materials. Melamine (99%, Sigma-Aldrich), Trizma base [tris(hydroxymethyl)aminomethane, ≥ 99.9%, Sigma-Aldrich], dopamine hydrochloride (Sigma-Aldrich), cobalt(II) nitrate hexahydrate (Alfa Aesar), 2-methylimidazole (2-MeIm, Sigma-Aldrich), potassium hydroxide (KOH, Merck KGaA), Nafion (5 wt.% in alcohol and water, Sigma-Aldrich), 20% platinum on carbon and 20% iridium on carbon (Alfa Aesar) were directly used as received.

Synthesis of carbon nitride (C_3N_4). Typically, melamine (10 g) was placed in a porcelain crucible and heated to 550 °C at a ramping rate of 5 °C/min and kept at 550 °C for 4 h under Ar atmosphere, to obtain C_3N_4 by thermal polymerization. The sample was naturally cooled to room temperature and C_3N_4 was obtained with a yield of approximately 50%.

Synthesis of ZIFCNDA electrocatalyst. Typically, a 0.45 mg cm^{-3} aqueous C_3N_4 solution was stirred for 30 minutes and then bath sonicated for 15 minutes. Subsequently, 75 mg of dopamine hydrochloride (0.3 mg cm^{-3} in the final solution) were added to the as-prepared C_3N_4 solution and stirred for 15 minutes. A solution containing $Co(NO_3)_2.6H_2O$ at a mole ratio of 2:1 ($Co(NO_3)_2.6H_2O$:Dopamine) was added to the previously prepared solution and stirred for 15 minutes. Then, 1.21 mg cm^{-3} of trizma base was added to the solution under vigorous stirring to trigger dopamine polymerisation. After 4 hours of mild stirring, 100 mL of an aqueous solution of 2-methylimidazole (0.35 mg cm^{-3}) was added and the mixture stirred for another 20 minutes. The product was finally collected by centrifugation (10 minutes at 8000 rpm) and repeatedly washed with deionized water and ethanol. After overnight oven drying, the material was pyrolyzed at 900 °C for 2h, at a ramping rate of 5 °C min^{-1} in N_2 atmosphere. For comparison, the intermediates, polydopamine (CPDA), carbon nitride/polydopamine (CNDA) and cobalt-doped carbon nitride/polydopamine (Co-CNDA) were synthesised following the procedure above; CPDA was prepared without the addition of C_3N_4, $Co(NO_3)_2.6H_2O$ and 2-methylimidazole; CNDA without the addition of $Co(NO_3)_2.6H_2O$ and 2-methylimidazole and Co-CNDA without the addition of 2-methylimidazole.

Characterization. The morphologies and elemental mappings of the products were obtained by Field Emission-Scanning Electron Microscope (FE-SEM, JSM-7600F), Transmission Electron Microscope (TEM, Philips CM300) and FEI G2 F20 X-Twin Transmission Electron Microscope (TEM), equipped with an Elite-T silicon drift detector (SDD) (1.0sr solid angle) for energy dispersive X-ray spectroscopic mapping (EDS). The chemical compositions were investigated by X-ray Photoelectron Spectroscopy (XPS) using a Theta Probe electron spectrometer (VG ESCALAB200i-XL, Thermo Scientific). The binding energies were calibrated using C 1s peak at 285 eV. The crystallinity and phase composition of the samples were studied by X-ray Diffraction (XRD, Bruker D8 Discover GADDS with a Cu K_α radiation). The Brunauer−Emmett−Teller (BET) surface area and pore size distribution were obtained from the nitrogen adsorption−desorption isotherms and the Barrett-Joyer-Halenda (BJH) method by using an Automatic High Resolution Physisorption Micropore/Mesopore Analyzer (ASAP2020MP MICROMERITICS).

Electrochemical measurements. The electrocatalytic activity of the synthesised catalysts was investigated by Cyclic Voltammetry (CV) and Linear Sweep Voltammetry (LSV) measurements acquired from a Metrohm Autolab potentiostat/galvanostat (PGSTAT302N) station using a three-electrode system consisting of an Ag/AgCl (in saturated KCl) reference electrode, a Pt foil as the counter electrode and a glassy carbon working electrode (GC, 5 mm diameter). 0.1 M KOH solution saturated with O_2 or N_2 was used as the electrolyte. The working electrode was prepared by addiиg 10 mg of catalyst to a solution containing 1.47 mL of deionised water, 0.73 ml of EtOH and 0.5 mL of Nafion (5 wt.% in alcohol and water) and sonicating it for 30 mins to obtain a homogenous ink. An aliquot (8.3 µL) of this ink was drop-cast onto the GC electrode surface to obtain a theoretical catalyst loading of 0.4 mg cm^{-2}, unless

otherwise stated. Pt/C and Ir/C electrodes were also prepared following the same procedure. From the LSV results, the number of electrons (n) transferred per O_2 molecule in ORR was calculated from the Koutecky-Levich (K-L) equation as follows:[28]

$$\frac{1}{J} = \frac{1}{J_L} + \frac{1}{J_K} = \frac{1}{B\omega^{1/2}} + \frac{1}{J_K} \quad (1)$$

$$B = 0.2nFC_0(D_0)^{2/3}\nu^{-1/6} \quad (2)$$

$$J_K = nFkC_0 \quad (3)$$

Where J is the measured current density, J_k and J_L are the kinetic limiting and diffusion limiting current densities, respectively, B is the Levich constant (determined by the inverse value of the slope of a straight linear fitting of the measured current densities, ω is the angular velocity of the electrode, F is the Faraday constant (96485 C mol^{-1}), C_0 is the concentration of dissolved O_2 in electrolyte solution (1.2×10^{-6} mol cm^{-3}), D_0 is the O_2 diffusion coefficient in KOH solution (1.9×10^{-5} cm^2 s^{-1}) and ν is the kinetic viscosity of the electrolyte solution (0.01 cm^2 s^{-1}).[7,29] Both CV and LSV measurements were recorded with reference to the Ag/AgCl electrode. The potentials recorded by Ag/AgCl reference electrode potentials were calibrated with respect to the RHE potential according to the Nernst equation:

$$E_{RHE} = E_{Ag/AgCl} + 0.059pH + E^o_{Ag/AgCl} \quad (4)$$

Where E_{RHE} is the potential converted, $E_{Ag/AgCl}$ is the experimentally measured potential against the Ag/AgCl reference, the measured pH was 13 and $E^o_{Ag/AgCl}$ = 0.1976 at 25 ˚C.

Assembly and testing of Zn-air batteries (ZABs). The Zn-air cells were assembled using a polished zinc plate as the anode, an air cathode containing the ZIFCNDA, Pt/C or Ir/C catalysts and a 6 M KOH aqueous solution containing 0.1 M $ZnCl_2$ as the electrolyte. For the preparation of the cathode ink, a solution containing 50 mg of active catalyst and 10 mL of an aqueous Nafion solution (1 wt.%) was sonicated for 30 min. Then, this solution with calculated amount was drop-casted onto a carbon paper (Sigracet 38BC) to obtain a catalyst loading of 0.5 mg cm^{-2}. The electrode was then dried overnight at room temperature. The discharge and discharge-charge performances of ZABs were evaluated by the galvanostatic method on a battery tester (NEWARE BTS-610).

RESULTS AND DISCUSSION

Figure 1 schematically details the synthetic procedure idea for the preparation of the ZIFCNDA catalyst. Firstly, dopamine hydrochloride and cobalt nitrate, $Co(NO_3)_2.6H_2O$, were added to a well-dispersed C_3N_4 solution yielding a light-pink coloured solution. Then, the addition of trizma base aimed to trigger the polymerization of dopamine along with the introduction of cobalt, forming a layered framework. Upon addition of the 2-MeIm ligand solution, the colour

instantly changed to blue-violet, suggesting the formation of ZIF-67. The synthesis of ZIF-67 involves the quick Co-N coordination bond formation when cobalt salt and 2-MeIm solutions are mixed. The instant colour change is indicative of the coordination reaction. Finally, high-temperature pyrolysis at 900°C yielded the formation of small particles scattered across the carbon sheets.

The morphologies of the composites at different stages of the process were examined by TEM in Figure 2 and Figure S1. The TEM image in Figure 2a shows the thin substrate layered structure (CNDA) formed by the growth-controlled polymerization of dopamine on a C_3N_4 template. During this polymerization process, cobalt ions were introduced to promote direct cobalt doping onto the carbon framework. Additionally, the 2-MeIM ligand was added to the solution to promote selective growth of Co-based MOF particles with a polyhedron-like structure (ZIF-67) and an average size of 900 nm, as observed in Figure S1a. The successful formation of ZIF-67 on the N-doped carbon-based scaffold was confirmed by the XRD pattern observed in Figure S2.[20] Following this, pyrolysis at 900°C under an N_2 atmosphere yielded a structure composed of nanoparticles with diameters ranging from about 20-40 nm evenly distributed on thin carbon layers (ZIFCNDA), as revealed in Figures 2b and S1c. In order to confirm the elemental distribution on the nanoparticles and the supporting framework, TEM with EDS elemental mapping profile was used (Fig. 2e-f). The layered framework was found to contain evenly distributed C, N and O and mostly Co was localised in the nanoparticle regions, confirming the formation of Co nanoparticles on a carbon support. Figures S1d and 1c-d reveal the formation of graphene-like carbon nanosheets catalysed by the introduction of cobalt nanoparticles.[29] Additionally, the TEM image obtained at a higher magnification (Figure 2c-d) showed that the Co NPs were supported by surrounding carbon shells. The FFT image (inset of Figure 2c) reveals the lattice fringes on the nanoparticles with d-spacings of about 0.20 nm and 0.18 nm correspondent to the (111) and (200) planes of face-centered cubic phase of metallic Co, respectively, whereas the lattice spacings of 0.34 nm were ascribed to the (002) plane of graphitized carbon surrounding the particles. During thermal activation, the organic moieties are gradually converted to graphitic carbon, causing the loss of hydrogen and some carbon and nitrogen atoms, altering the structure of the framework, along with pore formation. After thermal activation, the original ZIF structure cannot be retained, however, it is important to aid the uniform distribution of Co and N-functional groups.[30] This strategy allowed the metal particles to be well dispersed on the carbon substrate, reducing the formation of unstable loose crystals and restraining their aggregation while avoiding the need for the addition of any nanoparticle growth-control agents.[16,31] It was observed that if the 2-methylimidazole ligand is not added to promote the formation of Co-based MOFs, upon pyrolysis uneven nanoparticles and random aggregations are formed, encapsulating the nanoparticles, and therefore reducing the active sites exposure (Figure S1b).

In accordance with the TEM results, the XRD pattern of ZIFCNDA show diffraction peaks at around 26°, 44.2°, 51.5° and 75.9°, that could be attributed to the (002) plane of graphitic carbon and the (111), (200) and (220) planes of metallic Co, respectively (Figure 3a).[16,32] A shift towards higher angles of the C (002) peak at 21.5° of CNDA, assigned to amorphous carbon, indicates the formation of graphitized carbon in ZIFCNDA (Figure 3b) and confirms the essential role of Co in the formation of graphitic C.[20] The Co ions can catalytically promote the conversion of its coordinated organic linkers into graphitized carbon at high temperatures which may then enhance electrical conductivity.[20,33]

The surface area and pore structures were investigated by N_2 adsorption-desorption isotherms (Table S1). The ZIFCNDA catalyst shows a type IV isotherm with a hysteresis loop, suggesting the presence of mesopores (Figure 3c).[38,39] The ZIFCNDA catalyst presented a BET surface area of 268 $m^2\ g^{-1}$ that is larger than that of CPDA (64.1 $m^2\ g^{-1}$, Figure S4a), ascribed to the inclusion of C_3N_4 as a template for the controlled growth of the layered carbon framework, however the CNDA precursor presented a much larger BET surface area (1590 $m^2\ g^{-1}$, Figure S4b) than that of the ZIFCNDA catalyst, possibly due to complete decomposition of C_3N_4 in these samples (Figure S3). Furthermore, the Co NPs formed on the ZIFCNDA catalyst structure may promote the conversion of some organic linkers into the carbon matrix while others can be decomposed as smaller molecules.[20] The rapid N_2 uptake observed at $P/P_0 > 0.8$ for CNDA indicates the existence of larger pores.[26] The BJH desorption average pore radius of the investigated composite was found to be 3.10 nm (6.20 nm diameter), which can facilitate the electrolyte access to the catalytically active sites (Figure 3d). The pore size reduction in comparison to those of CPDA and CNDA might be due to the coverage of some pores/defects by Co NPs (Figure S4c-d). Moreover, according to the BJH, the pore volume of ZIFCNDA was found to be about 0.36 $cm^3\ g^{-1}$. As observed in previous studies the combination of ZIF-67-based nanoparticles and C_3N_4 originated bulky structures with random nanotubes, whereas our ZIF-67-based catalyst originated well-defined nanoparticles on a carbon support due to the presence a C_3N_4 template to allow the controlled growth of polydopamine.[16,26]

The elemental compositions and chemical states of ZIFCNDA were determined by XPS. The survey spectra indicated the presence of C, N and O on CPDA and CNDA and the further incorporation of Co in the developed ZIFCNDA catalyst (Figure 4a). In the high resolution C1s spectra of ZIFCNDA, four peaks were fitted at about 285.1 eV, 286.3 eV, 288 eV and 290.5 eV, corresponding to sp^2 C, C-O and C=N, C-O-C and C-N, respectively (Figure 4b).[40,41] These results were consistent with the C1s spectra of CPDA and CNDA observed in Figures S5a-b, confirming the essential presence of CPDA in the formation of a stable framework. The N1s XPS spectrum of ZIFCNDA (Figure 4c) was deconvoluted into a peak at 399.2 eV which includes contributions from the pyridinic N and N-Co binding energies (BE) and another one at 401.6 eV assigned to presence of graphitic N. The pyridinic N and N-Co peak binding energies are adjacent to one another and difficult to differentiate, the peak at 399.2 eV likely includes contributions from the both chemical environments.[42,43] Hence, a shift in the peak towards higher BE is observed in comparison to that of the pyridinic N peak of CPDA and CNDA due to the additional contribution of the N-Co (Figure S5c-d). The N on the graphitic carbon basal plane may attract Co ions to form the ZIF-67 structures.[26] The graphitic N peak did not suffer any shifts after incorporation of Co, confirmed by the comparison of the same peak of CPDA and CNDA with ZIFCNDA. Notably, the presence of pyridinic and graphitic N moieties are known to help improving the overall catalyst activity by promoting a favourable 4-electron pathway with a more positive onset potential and enhancing the limiting current density, respectively.[22,44,45] Figure 4d presents the Co 2p spectra of ZIFCNDA showing one main peak at 780.9 eV with a satellite peak at 786.2 eV and one main peak at 796.6 eV with a satellite peak at 803.3 eV, assignable to the Co $2p_{3/2}$ and Co $2p_{1/2}$ of Co^{2+}. The binding energy of the peaks at 780.9 eV 796.6 eV were close to those of Co-N reported for Co (II) porphyrin (cobalt ions and cross-linked N-based ligands) suggesting that the oxidized state of Co is coordinated with two adjacent atoms, indicating the formation of Co-N.[46–48] Since a higher stoichiometric ratio of C and N is required to form these sites than those available, some Co^{2+} may agglomerate as Co^0.

The electrocatalytic activity of the prepared catalysts towards ORR and OER was evaluated. Initially, the ORR performance was studied in O_2-saturated alkaline electrolyte (0.1 M KOH) by cyclic voltammetry (CV) as observed in Figure 5a. The final catalyst ZIFCNDA presented a positively shifted cathodic peak at 0.83 V vs. RHE, but no features were observed in the N_2-saturated electrolyte, confirming the oxygen reduction catalytic activity. The results were comparable to the peak of the benchmark Pt/C (20 wt.%) catalyst at 0.82 V vs. RHE, confirming the suitability of the electrocatalyst developed in this study. Linear sweep voltammetry (LSV) polarization curves of C_3N_4, CPDA, CNDA, Co-CNDA, ZIFCNDA and Pt/C tested by rotating disk electrode (RDE) are observed in Figure 5b. Clearly, the ZIFCNDA catalyst showed improved ORR activity when compared to its precursors, C_3N_4, CPDA, CNDA, Co-CNDA, as observed by the greatly improved half-wave potential ($E_{1/2}$) and limiting current density. The ZIFCNDA presented a positively shifted $E_{1/2}$ of 0.84 V and a limiting current density of 4.21 mA cm^{-2}, a comparable catalytic activity to the commercial Pt/C with a half-wave potential of 0.86 V and limiting current density of 4.43 mA cm^{-2}. These results imply an improved mass transport pathway and an increased concentration of active sites promoting O_2 adsorption and reduction. The synergistic effect between layered carbon shells and Co NPs may facilitate the electron transfer to the catalytically active sites and improve stability.[29,43] The OER performance of the ZIFCNDA catalyst was evaluated following the ORR tests in the same 0.1 M KOH solution and the results compared to the commercial catalyst Ir/C. As presented in Figure 5c, the ZIFCNDA electrocatalyst achieved a current density as high as the benchmark OER catalyst, Ir/C, about 11.6 mA cm^{-2}, despite a higher anodic onset potential. Both CNDA and Co-CNDA precursors reached a much lower current density and a higher onset potential than the ZIFCNDA catalyst, confirming the essential contribution of the ZIF-67-based Co NPs for an improved OER performance and its promising use for rechargeable ZABs. The electrochemically active surface area (ECSA) is proportional to the electrochemical double-layer capacitance (C_{dl}) at the catalyst-electrolyte interface and can be measured by cyclic voltammetry obtained at different scan rates at non-Faradaic potentials.[49] As observed in Figure S6 the notably higher C_{dl} value of ZIFCNDA of 74.9 mF cm^{-2} than of the benchmark Pt/C catalyst of 12.8 mF cm^{-2} are in good agreement with the ZIFCNDA catalyst's superior activity due to more exposed active sites. In order to further understand the ORR activity of the catalysts, ORR polarization curves were collected at different rotation speeds (Figure S7). Koutecky-Levich (K-L) relations were deduced from the measured current densities and the number of electrons transferred per oxygen molecule (n) was determined (Figure 5d). The K-L plots showed a wide and steady plateau suggesting a diffusion-controlled ORR and linear and parallel slopes suggesting first-order reaction kinetics with respect to the concentration of O_2 dissolved in the electrolyte. The average n value for the potential range of 0.2-0.6 V vs. RHE was calculated to be of 3.9 for the ZIFCNDA catalyst, higher than an n value of 3.7, calculated for CNDA, suggesting an improved electron transport upon inclusion of the cobalt-based nanoparticles (Figure S7). This was also comparable to the theoretical value of 4 for the Pt/C benchmark catalyst, suggesting a favourable 4-electron transfer pathway by avoiding the production of detrimental hydroperoxide.[22] The long-term stability of the developed catalyst towards the ORR was analysed by chronoamperometric (current vs. time, *i-t*) experiments. The results presented in Figure 5e show that the ZIFCNDA catalyst was able to retain 96.8 % of its initial current after 15000 minutes at 0.4 V with a continuous O_2 flow. Despite being the benchmark catalyst for ORR, Pt/C was only able to conserve 83.8 % of its initial current after the same period of time. The methanol tolerance of the studied catalyst was also evaluated by

chronoamperometric measurements. As presented in Figure 5f, upon addition of 5 mL of methanol to the O_2-saturated alkaline electrolyte only a slightly reduction in the current density was observed for the ZIFCNDA catalyst, whereas a sharp drop in current was detected for the Pt/C. These results further confirm the enhanced selectivity towards ORR of the developed catalyst and resistance to methanol crossover. Furthermore, the accelerated degradation tests (ADT) confirmed the durability of the ZIFCNDA catalyst since its LSV curve (Figure S8) only shifted by 10 mV at a current density of – 1 mA cm^{-2} after 400 cycles.

Figure S9 shows the polarization and power density curves of the ZABs containing the ZIFCNDA and Pt/C electrocatalysts. The Pt/C-based cell achieved a maximum power density of 43 mW cm^{-2} at a current density 54 mA cm^{-2} but the addition of the ZIFCNDA electrocatalyst to the air cathode resulted in a cell activity improvement, which achieved a power density of 57 mW cm^{-2} at a current density 71 mA cm^{-2}. Furthermore, the ZIFCNDA- and Pt/C-based ZABs were discharged at different current loads (5, 10 and 15 mA cm^{-2}) to evaluate their durability (Figure S10a-c). At all three current densities, the ZIFCNDA-based tested batteries presented similar flat discharge voltage plateaus to that of their Pt/C counterpart. In all long-term discharge plots the ZIFCNDA-based ZABs discharging time surpassed that of the Pt/C-based cells. Upon discharge at 5 mA cm^{-2} (Fig. S10a), the ZIFCNDA-based battery showed a similar initial discharge voltage to that of the Pt/C-based ZAB (1.24 V vs. 1.30 V) and achieved a maximum discharging time at nearly 600 h, 100 h longer than that observed for Pt/C, in good agreement with the slower cell degradation and increased cell-life showed during galvanostatic cycling. Additionally, the ZIFCNDA-based battery demonstrated a specific capacity of 686 mAh g^{-1} (normalized to the mass of consumed Zn), higher than that observed for the battery containing the commercial Pt/C 570 mAh g^{-1} (Figure S10d). The galvanostatic discharge plots of the ZIFCNDA-containing ZABs at increasing current densities (Figure S11) presented stable, flat and higher discharge voltage plateaus, particularly at 30 mA cm^{-2} when a high discharge voltage of 1.14 V was achieved, in comparison to 1.11 V of Pt/C.

Zinc-air batteries containing the developed ZIFCNDA or the benchmark electrocatalysts (e.g. Pt/C or Ir/C) as the air-cathode were prepared and subjected to galvanostatic discharge-charge cycling at 10 mA cm^{-2} or 15 mA cm^{-2} (Figure 6a and S12). When a current density of 10 mA cm^{-2} is applied, the ZIFCNDA-based ZAB presented great stability and rechargeability for over 150 h, much longer than the life cycle of the Pt/C and Ir/C-based Zn-air batteries (7 h and 30 h). An initial voltage gap of 1.03 V was observed for the ZIFCNDA-driven ZAB, obtained from discharge and charge voltages of 1.11 V and 2.14 V respectively, comparable to the Ir/C containing battery and superior to the Pt/C-based battery, which presented a larger voltage gap of 1.24 V (Figure 6b). After 25 h, the battery containing the Ir/C electrocatalyst started degrading, increasing its voltage gap up to 1.38 V, while the ZIFCNDA-based ZAB suffered a slight voltage gap broadening of 30 mV, confirming its greater durability. Finally, after 300 cycles (approximately 150 h), the ZIFCNDA-based battery was able to continue to cycle with a voltage gap of 1.19 V, provided by a discharging voltage of 1.06 V and a charging voltage of 2.25 V (Figure 6c). The final discharge voltage suffered a mere drop of 50 mV while the charge voltage increased by 110 mV, leading to an overall increase in the voltage gap of only 164 mV than in the first cycle. Remarkably, even at a current of 15 mA cm^{-2} the ZIFCNDA-based ZAB was able to cycle at a reasonably constant voltage gap for 65 h, whereas the battery with the Ir/C catalyst quickly degraded after only 15 h, with the Pt/C-based cell struggling to charge throughout (Figure S12).The reduced overpotentials reflect the greater energy efficiency and

bifunctional activity of the prepared catalyst, which reduce the degradation of the catalyst and consequently increase the battery-life.

CONCLUSION

In summary, we have developed an efficient bifunctional electrocatalyst composed of naturally dispersed Co NPs surrounded by graphitic carbon shells on a N-doped g-carbon substrate. Our simplified strategy involved the introduction of Co ions along with the polymerisation of dopamine, leading to the direct doping of the carbon framework and further localized growth of Co-based MOFs polyhedrons which then generated Co-based NPs upon pyrolysis. Furthermore, the addition of C_3N_4 controlled the polydopamine growth to form thin carbon nanosheets which could then be graphitized during high temperature annealing, helping to facilitate the electron transfer to the catalytically active sites. This approach also restrained the formation of unstable loose particles while also preventing their aggregation and generating a porous structure. The ZIFCNDA catalyst presented an improved activity in comparison to the benchmark ORR and OER catalysts, Pt/C and Ir/C, respectively. The essential contribution of the Co NPs for a great bifunctional activity was demonstrated by the poor activity of the nanoparticles-free composite (CNDA) and Co-CNDA, which also confirmed the essential addition of the 2-MeIM ligand for the formation of stable Co NPs. The ZIFNCDA-containing ZABs presented an outstanding activity during the long-term discharge analysis at 5 mA cm^{-2}, reaching a 600 h maximum discharging time, 100 h longer than the Pt/C benchmark as well as a higher specific capacity of 686 mAh g^{-1}. The cell was able to cycle for 150 h at 10 mA cm^{-2} with a mere increase in the voltage gap of 164 mV and even at a higher current density of 15 mA cm^{-2}, the ZIFCNDA-based cell was able to cycle at a constate voltage for 65 h, surpassing both Pt/C and Ir/C based cells.

ACKNOWLEDGMENTS

This research was supported by the University College London (UCL) and Agency for Science, Technology and Research (A*STAR), Singapore Research Attachment Programme (ARAP). The authors thank Dr. Lim Poh Chong (IMRE) for his help with XRD data collection, Dr. Jisheng Pan (IMRE) for his help with XPS data collection, Dr Lin Ming and Ms. Siew Lang Teo (IMRE) for their help with TEM characterization and Ms. Xiping Ni for her help with BET data collection.

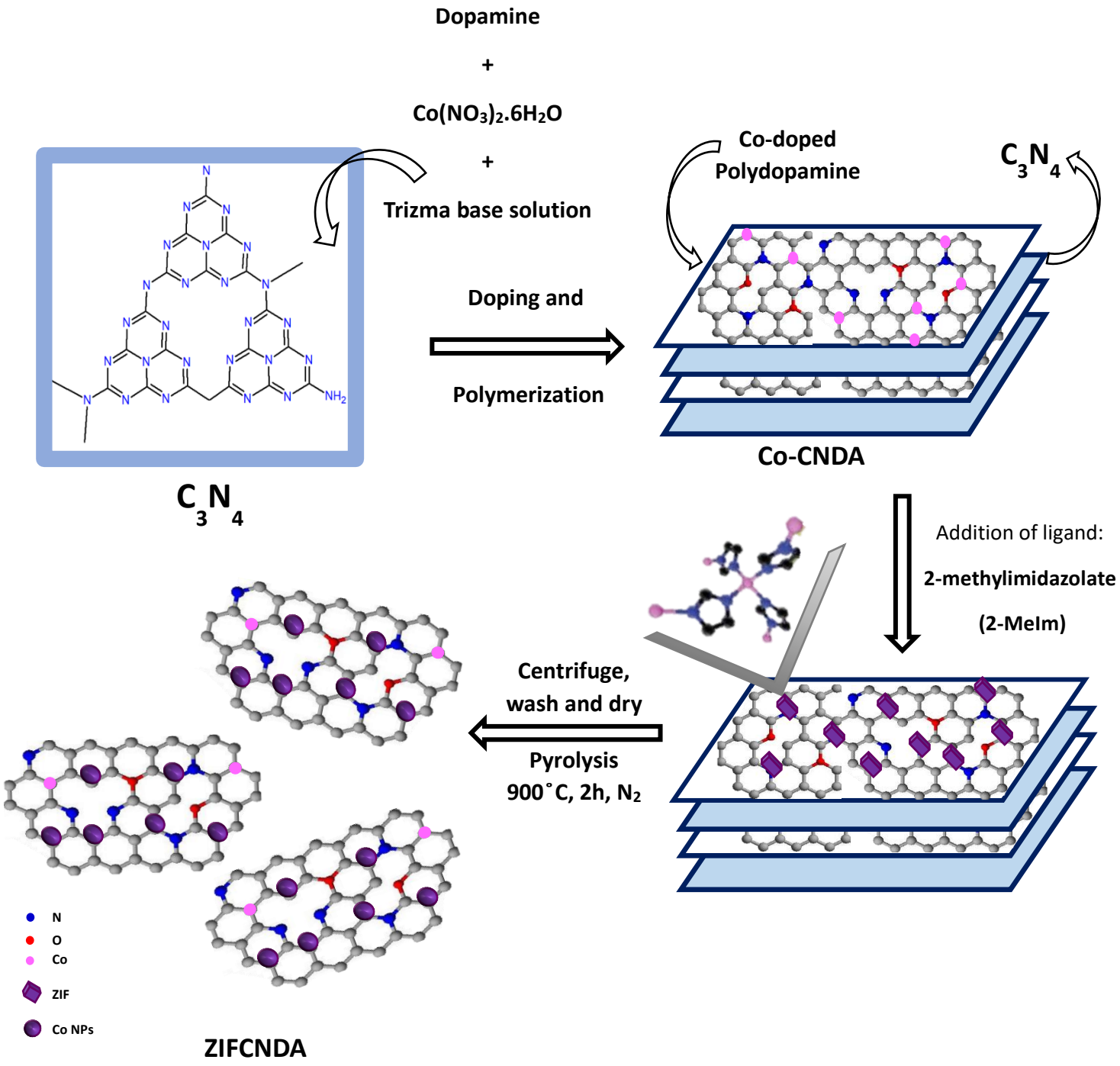

Figure 1: Schematic illustration of the synthesis of the ZIFCNDA catalyst.

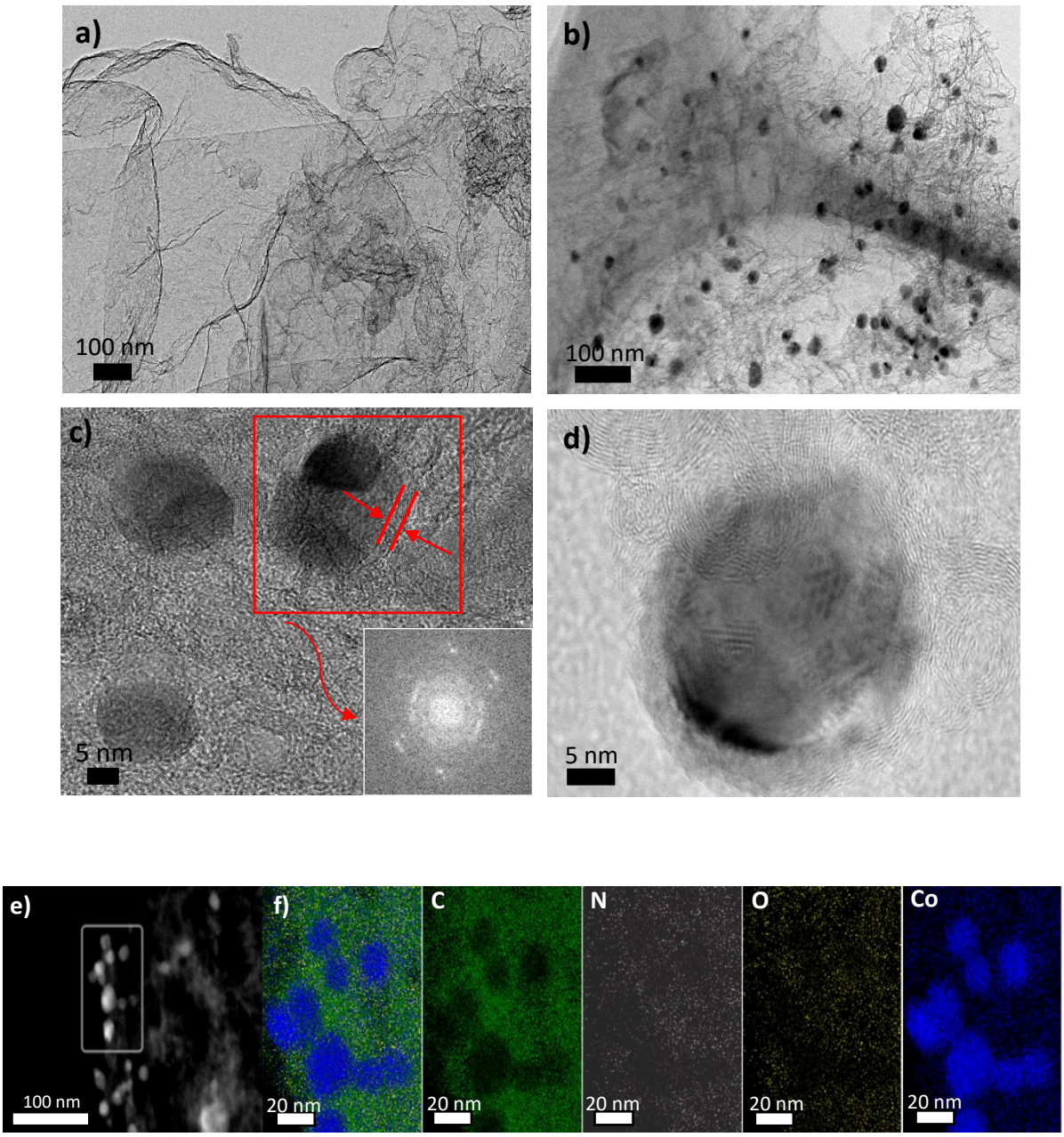

Figure 2: TEM images of a) CNDA and b) ZIFCNDA; c-e) HRTEM images of ZIFCNDA (inset: corresponding FFT) and f) corresponding elemental mapping images of e).

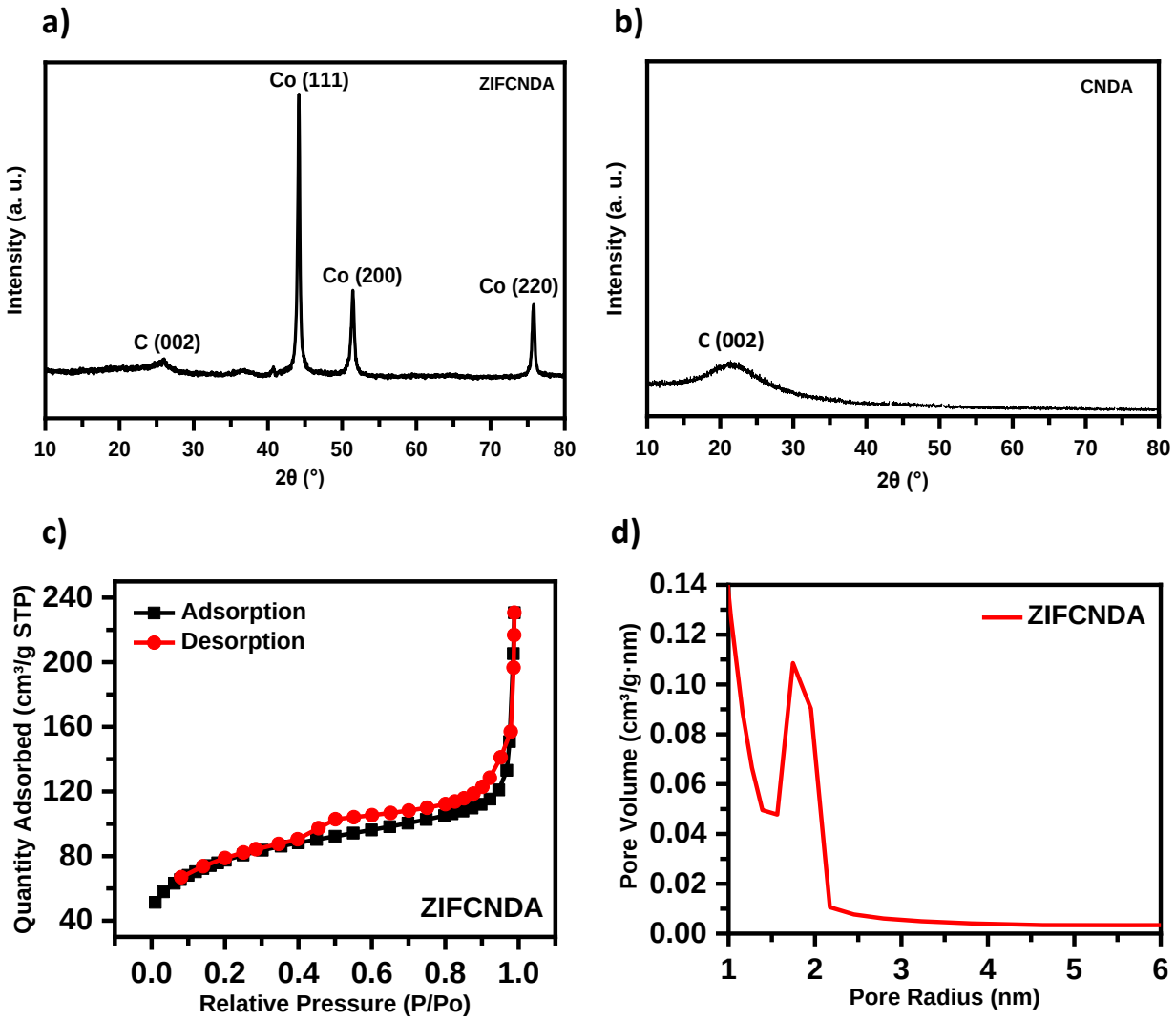

Figure 3: a) XRD pattern of ZIFCNDA and b) CNDA; c) N_2 adsorption-desorption isotherms of ZIFCNDA and d) corresponding BJH pore distributions.

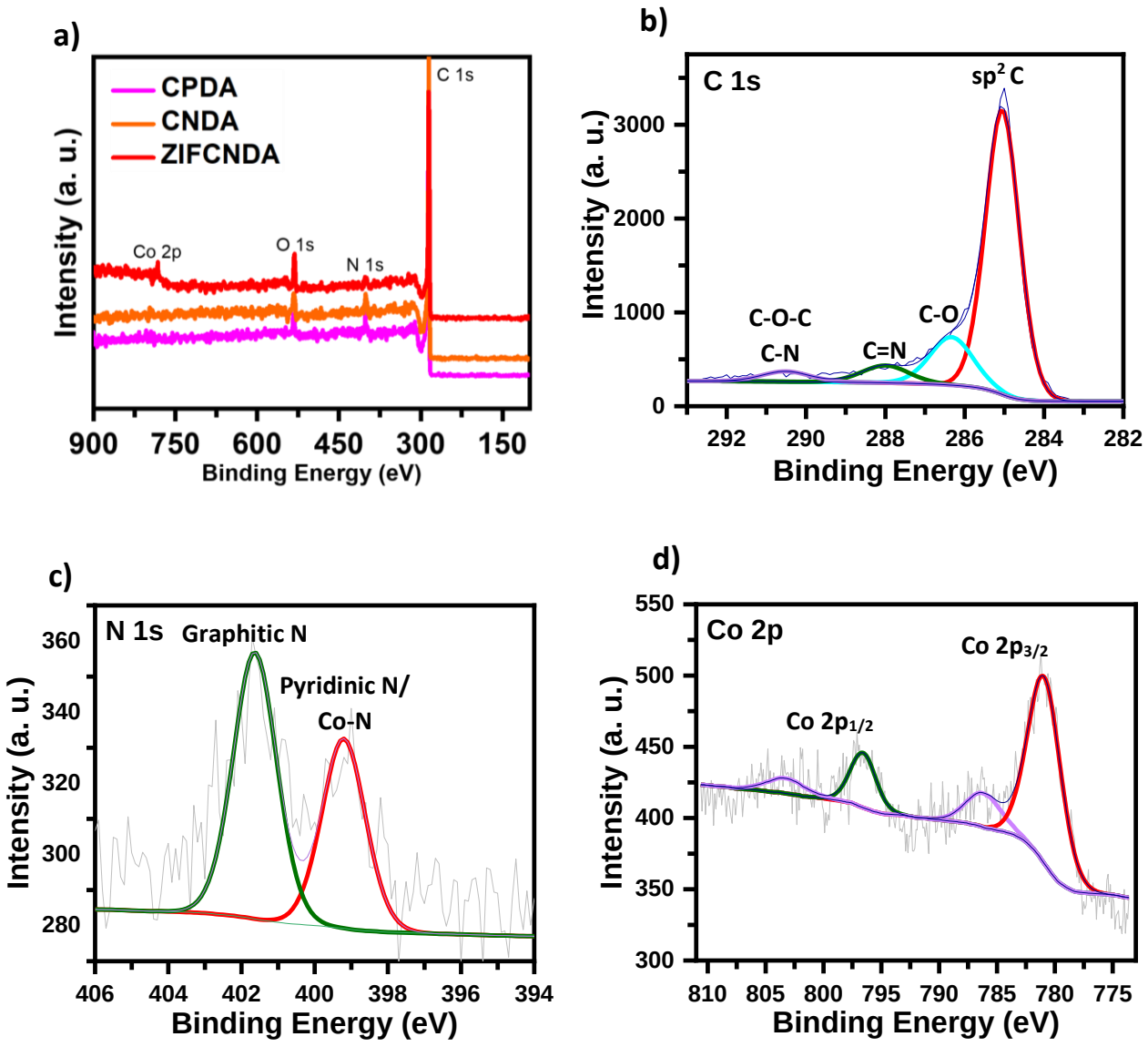

Figure 4: a) XPS survey spectra of CPDA, CNDA and ZIFCNDA; and the high-resolution spectrum for b) C 1s, c) N 1s and d) Co 2p of ZIFCNDA.

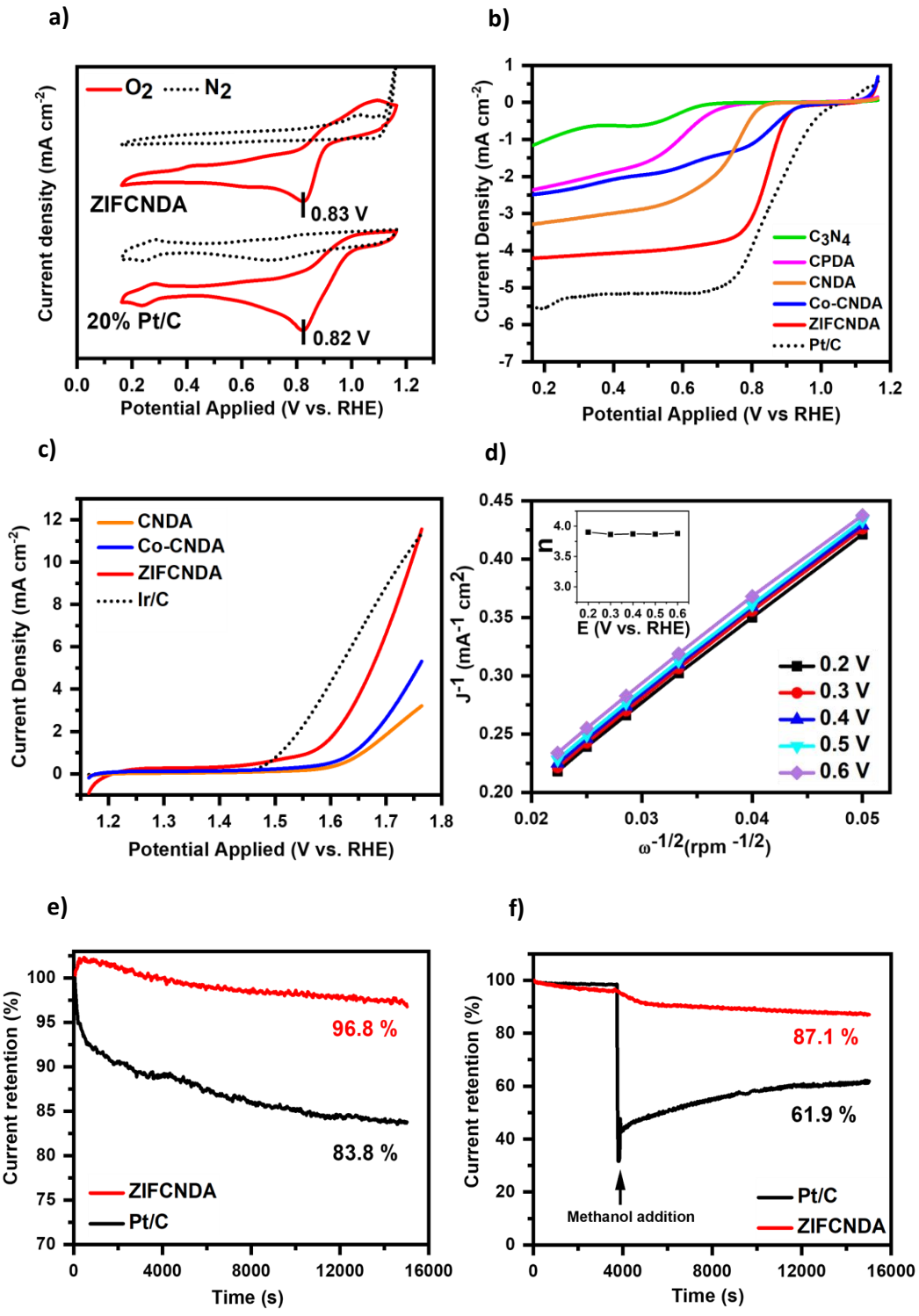

Figure 5: a) CV curves of the ZIFCNDA catalyst and Pt/C obtained in N_2/O_2-saturated 0.1 M KOH electrolyte. b) Combined LSV curves for ORR of the ZIFCNDA catalyst, Co-CNDA, CNDA CPDA, C_3N_4 and Pt/C at 1600 rpm in O_2-saturated 0.1 M KOH electrolyte. c) Combined LSV curves for OER of ZIFCNDA, Co-CNDA and CNDA in 0.1 M KOH electrolyte. d) K-L plots of ZIFCNDA calculated from its RDE LSV curves at the potential range 0.2-0.6 V vs. RHE; the inset: plot of n (electron transfer number) per O_2 molecule at the different potentials. e) Chronoamperometric stability plots (i-t plots) of ZIFCNDA and Pt/C at 0.4 V and a fixed electrode rotation speed of 400 rpm in O_2-saturated 0.1 M KOH electrolyte. f) I-t plots of ZIFCNDA and Pt/C at 0.4 V and a fixed electrode rotation speed of 400 rpm in O_2-saturated 0.1 M KOH electrolyte with addition of 5 mL MeOH. The scan rate was kept at 5 mV s^{-1} for all the measurements.

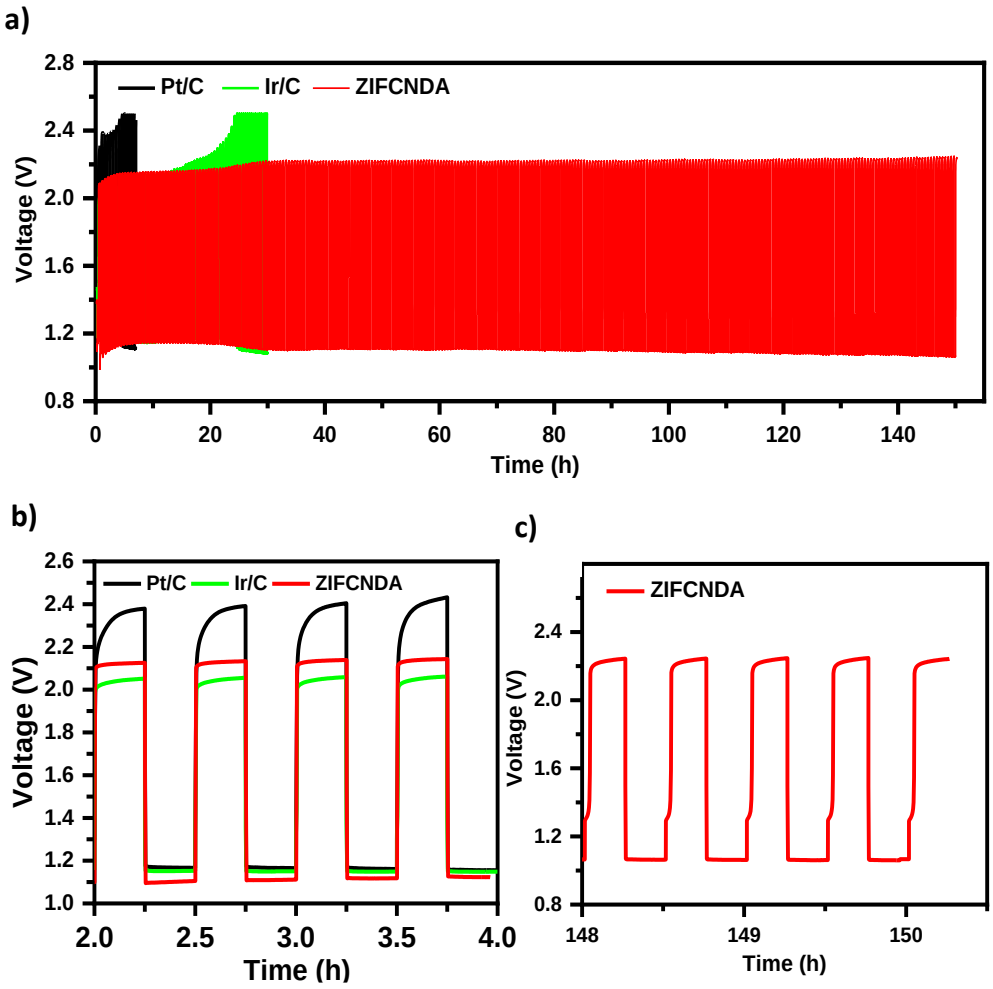

Figure 6: a) Discharge-charge cycling performances of ZABs with ZIFCNDA, Pt/C and Ir/C catalyst at 10 mA cm^{-2}. b and c) Selected sections of the cycling performances from c). All cells were prepared with a mass loading of 0.5 mg cm^{-2} and tested in 6 M KOH electrolyte at scan rate of 5 mV s^{-1}.

REFERENCES

(1) Cao, R.; Lee, J. S.; Liu, M.; Cho, J. Recent Progress in Non-Precious Catalysts for Metal-Air Batteries. *Adv. Energy Mater.* **2012**, *2* (7), 816–829. https://doi.org/10.1002/aenm.201200013.

(2) Pan, J.; Xu, Y. Y.; Yang, H.; Dong, Z.; Liu, H.; Xia, B. Y. Advanced Architectures and Relatives of Air Electrodes in Zn – Air Batteries. **2018**, *1700691*. https://doi.org/10.1002/advs.201700691.

(3) Ren, S.; Duan, X.; Liang, S.; Zhang, M.; Zheng, H. Bifunctional Electrocatalysts for Zn-Air Batteries: Recent Developments and Future Perspectives. *J. Mater. Chem. A* **2020**, *8* (13), 6144–6182. https://doi.org/10.1039/c9ta14231b.

(4) Zhang, B.; Zheng, X.; Voznyy, O.; Comin, R.; Bajdich, M.; García-Melchor, M.; Han, L.; Xu, J.; Liu, M.; Zheng, L.; De Arquer, F. P. G.; Dinh, C. T.; Fan, F.; Yuan, M.; Yassitepe, E.; Chen, N.; Regier, T.; Liu, P.; Li, Y.; De Luna, P.; Janmohamed, A.; Xin, H. L.; Yang, H.; Vojvodic, A.; Sargent, E. H. Homogeneously Dispersed Multimetal Oxygen-Evolving Catalysts. *Science (80-.).* **2016**, *352* (6283), 333–337. https://doi.org/10.1126/science.aaf1525.

(5) Xia, B. Y.; Yan, Y.; Li, N.; Wu, H. Bin; Lou, X. W. D.; Wang, X. A Metal-Organic Framework-Derived Bifunctional Oxygen Electrocatalyst. *Nat. Energy* **2016**, *1* (1), 1–8. https://doi.org/10.1038/nenergy.2015.6.

(6) Li, J.; Kang, Y.; Liu, D.; Lei, Z.; Liu, P. Nitrogen-Doped Graphitic Carbon-Supported Ultrafine Co Nanoparticles as an Efficient Multifunctional Electrocatalyst for HER and Rechargeable Zn-Air Batteries. *ACS Appl. Mater. Interfaces* **2020**, *12* (5), 5717–5729. https://doi.org/10.1021/acsami.9b18101.

(7) Wang, Y.; Cao, Q.; Guan, C.; Cheng, C. Recent Advances on Self-Supported Arrayed Bifunctional Oxygen Electrocatalysts for Flexible Solid-State Zn–Air Batteries. *Small* **2020**, *16* (33), 1–20. https://doi.org/10.1002/smll.202002902.

(8) Reier, T.; Nong, H. N.; Teschner, D.; Schlögl, R.; Strasser, P. Electrocatalytic Oxygen Evolution Reaction in Acidic Environments – Reaction Mechanisms and Catalysts. *Adv. Energy Mater.* **2017**, *7* (1). https://doi.org/10.1002/aenm.201601275.

(9) Li, F.; Shu, H.; Liu, X.; Shi, Z.; Liang, P.; Chen, X. Electrocatalytic Activity and Design Principles of Heteroatom-Doped Graphene Catalysts for Oxygen-Reduction Reaction. *J. Phys. Chem. C* **2017**, *121* (27), 14434–14442. https://doi.org/10.1021/acs.jpcc.7b03093.

(10) Zhu, Y. P.; Liu, Y.; Liu, Y. P.; Ren, T. Z.; Du, G. H.; Chen, T.; Yuan, Z. Y. Heteroatom-Doped Hierarchical Porous Carbons as High-Performance Metal-Free Oxygen Reduction Electrocatalysts. *J. Mater. Chem. A* **2015**, *3* (22), 11725–11729. https://doi.org/10.1039/c5ta01611h.

(11) Tang, C.; Zhang, Q. Nanocarbon for Oxygen Reduction Electrocatalysis: Dopants, Edges, and Defects. *Adv. Mater.* **2017**, *29* (13). https://doi.org/10.1002/adma.201604103.

(12) Xue, W.; Zhou, Q.; Cui, X.; Jia, S.; Zhang, J.; Lin, Z. Metal–Organic Frameworks-Derived Heteroatom-Doped Carbon Electrocatalysts for Oxygen Reduction Reaction. *Nano Energy* **2021**, *86* (May), 106073. https://doi.org/10.1016/j.nanoen.2021.106073.

(13) Jiao, Y.; Zheng, Y.; Jaroniec, M.; Qiao, S. Z. Design of Electrocatalysts for Oxygen- and Hydrogen-Involving Energy Conversion Reactions. *Chem. Soc. Rev.* **2015**, *44* (8), 2060–2086. https://doi.org/10.1039/c4cs00470a.

(14) Zheng, Y.; Jiao, Y.; Zhu, Y.; Cai, Q.; Vasileff, A.; Li, L. H.; Han, Y.; Chen, Y.; Qiao, S. Z. Molecule-Level g-C3N4 Coordinated Transition Metals as a New Class of Electrocatalysts for Oxygen Electrode Reactions. *J. Am. Chem. Soc.* **2017**, *139* (9), 3336–3339. https://doi.org/10.1021/jacs.6b13100.

(15) Fu, T.; Li, G.; Xiang, Y.; Tang, Y.; Cai, D.; Jiang, S.; Xue, Y.; Xiong, Z.; Si, Y.; Guo, C. Hierarchical Cobalt-Nitrogen-Doped Carbon Composite as Efficiently Bifunctional Oxygen Electrocatalyst for Rechargeable Zn-Air Batteries. *J. Alloys Compd.* **2021**, *878*, 160349. https://doi.org/10.1016/j.jallcom.2021.160349.

(16) Wu, J.; Hu, L.; Wang, N.; Li, Y.; Zhao, D.; Li, L.; Peng, X.; Cui, Z.; Ma, L. J.; Tian, Y.; Wang, X. Surface Confinement Assisted Synthesis of Nitrogen-Rich Hollow Carbon Cages with Co Nanoparticles as Breathable Electrodes for Zn-Air Batteries. *Appl. Catal. B Environ.* **2019**, *254* (March), 55–65. https://doi.org/10.1016/j.apcatb.2019.04.064.

(17) Bai, Y.; Yang, D.; Yang, M.; Chen, H.; Liu, Y.; Li, H. Nitrogen/Cobalt Co-Doped Mesoporous Carbon Microspheres Derived from Amorphous Metal-Organic Frameworks as a Catalyst for the Oxygen Reduction Reaction in Both Alkaline and Acidic Electrolytes. *ChemElectroChem* **2019**, *6* (9), 2546–2552. https://doi.org/10.1002/celc.201900343.

(18) Wu, Y.; Wu, X.; Tu, T.; Zhang, P.; Li, J.; Zhou, Y.; Huang, L.; Sun, S. Controlled Synthesis of FeNx-CoNx Dual Active Sites Interfaced with Metallic Co Nanoparticles as Bifunctional Oxygen Electrocatalysts for Rechargeable Zn-Air Batteries. *Appl. Catal. B Environ.* **2020**, *278* (June), 119259. https://doi.org/10.1016/j.apcatb.2020.119259.

(19) Bai, Q.; Shen, F.; Li, S.; Liu, J.; Dong, L.; Wang, Z.; Lan, Y. Cobalt@Nitrogen-Doped Porous Carbon Fiber Derived from the Electrospun Fiber of Bimetal–Organic Framework for Highly Active Oxygen Reduction. *Small Methods* **2018**, *2* (12), 1800049. https://doi.org/10.1002/smtd.201800049.

(20) Tang, J.; Salunkhe, R. R.; Zhang, H.; Malgras, V.; Ahamad, T.; Alshehri, S. M.; Kobayashi, N.; Tominaka, S.; Ide, Y.; Kim, J. H. Bimetallic Metal-Organic Frameworks for Controlled Catalytic Graphitization of Nanoporous Carbons. *Nat. Publ. Gr.* **2016**, No. April, 3–4. https://doi.org/10.1038/srep30295.

(21) Wagia, R.; Strashnov, I.; Anderson, M. W.; Attfield, M. P. Insight and Control of the Crystal Growth of Zeolitic Imidazolate Framework ZIF-67 by Atomic Force Microscopy and Mass Spectrometry. *Cryst. Growth Des.* **2018**, *18* (2), 695–700. https://doi.org/10.1021/acs.cgd.7b01058.

(22) Li, B.; Igawa, K.; Chai, J.; Chen, Y.; Wang, Y.; Fam, D. W.; Tham, N. N.; An, T.; Konno, T.; Sng, A.; Liu, Z.; Zhang, H.; Zong, Y. String of Pyrolyzed ZIF-67 Particles on Carbon Fibers for High-Performance Electrocatalysis. *Energy Storage Mater.* **2020**, *25* (April 2019), 137–144. https://doi.org/10.1016/j.ensm.2019.10.021.

(23) Wang, G.; Deng, J.; Yan, T.; Zhang, J.; Shi, L.; Zhang, D. Turning on Electrocatalytic Oxygen Reduction by Creating Robust Fe-N: X Species in Hollow Carbon Frameworks via in Situ Growth of Fe Doped ZIFs on g-C3N4. *Nanoscale* **2020**, *12* (9), 5601–5611. https://doi.org/10.1039/d0nr00138d.

(24) Zheng, L.; Yu, S.; Lu, X.; Fan, W.; Chi, B.; Ye, Y.; Shi, X.; Zeng, J.; Li, X.; Liao, S. Two-Dimensional Bimetallic Zn/Fe-Metal-Organic Framework (MOF)-Derived Porous Carbon Nanosheets with a High Density of Single/Paired Fe Atoms as High-Performance Oxygen Reduction Catalysts. *ACS Appl. Mater. Interfaces* **2020**, *12* (12), 13878–13887. https://doi.org/10.1021/acsami.9b22577.

(25) Zhu, Y. P.; Guo, C.; Zheng, Y.; Qiao, S. Z. Surface and Interface Engineering of Noble-Metal-Free Electrocatalysts for Efficient Energy Conversion Processes. *Acc. Chem. Res.* **2017**, *50* (4), 915–923. https://doi.org/10.1021/acs.accounts.6b00635.

(26) Wang, R.; Yan, T.; Han, L.; Chen, G.; Li, H.; Zhang, J.; Shi, L.; Zhang, D. Tuning the Dimensions and Structures of Nitrogen-Doped Carbon Nanomaterials Derived from Sacrificial g-C3N4/Metal-Organic Frameworks for Enhanced Electrocatalytic Oxygen Reduction. *J. Mater. Chem. A* **2018**, *6* (14), 5752–5761. https://doi.org/10.1039/c8ta00439k.

(27) Hao, Y.; Xu, Y.; Liu, J.; Sun, X. Nickel-Cobalt Oxides Supported on Co/N Decorated Graphene as an Excellent Bifunctional Oxygen Catalyst. *J. Mater. Chem. A* **2017**, *5* (11), 5594–5600. https://doi.org/10.1039/c7ta00299h.

(28) Bard, A. J.; Faulkner, L. R. *Electrochemical Methods: Fundamentals and Applications*; 2001; Vol. 2nd ed. https://doi.org/10.1021/ed060pa25.1.

(29) Gao, L.; Zhang, M.; Zhang, H.; Zhang, Z. Cobalt-Carbon Nanocage Modified Carbon Foam as the Efficient Catalyst towards Oxygen Reduction Reaction and High-Performance Zinc-Air Battery. *J. Power Sources* **2020**, *450* (June 2019), 227577. https://doi.org/10.1016/j.jpowsour.2019.227577.

(30) Ma, S.; Goenaga, G. A.; Call, A. V.; Liu, D. J. Cobalt Imidazolate Framework as Precursor for Oxygen Reduction Reaction Electrocatalysts. *Chem. - A Eur. J.* **2011**, *17* (7), 2063–2067. https://doi.org/10.1002/chem.201003080.

(31) Wang, D.; Yang, P.; Xu, H.; Ma, J.; Du, L.; Zhang, G. X.; Li, R.; Jiang, Z.; Li, Y.; Zhang, J.; An, M. The Dual-Nitrogen-Source Strategy to Modulate a Bifunctional Hybrid Co/Co–N–C Catalyst in the Reversible Air Cathode for Zn-Air Batteries. *J. Power Sources* **2021**, *485* (November 2020), 229339. https://doi.org/10.1016/j.jpowsour.2020.229339.

(32) Ma, L.; Wang, R.; Li, Y. H.; Liu, X. F.; Zhang, Q. Q.; Dong, X. Y.; Zang, S. Q. Apically Co-Nanoparticles-Wrapped Nitrogen-Doped Carbon Nanotubes from a Single-Source MOF for Efficient Oxygen Reduction. *J. Mater. Chem. A* **2018**, *6* (47), 24071–24077. https://doi.org/10.1039/c8ta08668k.

(33) Chen, Y. Z.; Wang, C.; Wu, Z. Y.; Xiong, Y.; Xu, Q.; Yu, S. H.; Jiang, H. L. From Bimetallic Metal-Organic Framework to Porous Carbon: High Surface Area and Multicomponent Active Dopants for Excellent Electrocatalysis. *Adv. Mater.* **2015**, *27* (34), 5010–5016. https://doi.org/10.1002/adma.201502315.

(34) Gu, W.; Hu, L.; Li, J.; Wang, E. Hybrid of G-C3N4 Assisted Metal-Organic Frameworks and Their Derived High-Efficiency Oxygen Reduction Electrocatalyst in the Whole PH Range. *ACS Appl. Mater. Interfaces* **2016**, *8* (51), 35281–35288. https://doi.org/10.1021/acsami.6b12031.

(35) Zhang, M.; Wang, C.; Yan, X.; Kwame, K. P.; Chen, S.; Xiao, C.; Qi, J.; Sun, X.; Wang, L.; Li, J. Metal Organic Framework-Derived Hollow Cactus-like Carbon Sheets for Oxygen Reduction. *J. Mater. Chem. A* **2019**, *7* (35), 20162–20168. https://doi.org/10.1039/c9ta06609h.

(36) Loh, G. C.; Baillargeat, D. Graphitization of Amorphous Carbon and Its Transformation Pathways. *J. Appl. Phys.* **2013**, *114* (3). https://doi.org/10.1063/1.4816313.

(37) Rodríguez-Manzo, J. A.; Pham-Huu, C.; Banhart, F. Graphene Growth by a Metal-Catalyzed Solid-State Transformation of Amorphous Carbon. *ACS Nano* **2011**, *5* (2), 1529–1534. https://doi.org/10.1021/nn103456z.

(38) Wang, Y.; Zhong, K.; Huang, Z.; Chen, L.; Dai, Y.; Zhang, H.; Su, M.; Yan, J.; Yang, S.; Li, M.; Xu, T.; Tang, J. Novel G-C3N4 Assisted Metal Organic Frameworks Derived High Efficiency Oxygen Reduction Catalyst in Microbial Fuel Cells. *J. Power Sources* **2020**, *450* (January), 227681. https://doi.org/10.1016/j.jpowsour.2019.227681.

(39) Graphene, N.; Xu, L.; Tian, Y.; Deng, D.; Li, H.; Zhang, D. Cu Nanoclusters / FeN4 Amorphous Composites with Dual Active Cu Nanoclusters / FeN 4 Amorphous Composites with Dual Active Sites in N-Doped Graphene for High-Performance Zn-Air Batteries. **2020**. https://doi.org/10.1021/acsami.0c03823.

(40) Ai, K.; Liu, Y.; Ruan, C.; Lu, L.; Lu, G. Sp2 C-Dominant N-Doped Carbon Sub-Micrometer Spheres with a Tunable Size: A Versatile Platform for Highly Efficient Oxygen-Reduction

Catalysts. *Adv. Mater.* **2013**, *25* (7), 998–1003. https://doi.org/10.1002/adma.201203923.

(41) Li, R.; Parvez, K.; Hinkel, F.; Feng, X.; Müllen, K. Bioinspired Wafer-Scale Production of Highly Stretchable Carbon Films for Transparent Conductive Electrodes. *Angew. Chemie - Int. Ed.* **2013**, *52* (21), 5535–5538. https://doi.org/10.1002/anie.201300312.

(42) Zang, W.; Sumboja, A.; Ma, Y.; Zhang, H.; Wu, Y.; Wu, S.; Wu, H.; Liu, Z.; Guan, C.; Wang, J.; Pennycook, S. J. Single Co Atoms Anchored in Porous N-Doped Carbon for Efficient Zinc-Air Battery Cathodes. *ACS Catal.* **2018**, *8* (10), 8961–8969. https://doi.org/10.1021/acscatal.8b02556.

(43) Yang, F.; Chen, Y.; Cheng, G.; Chen, S.; Luo, W. Ultrathin Nitrogen-Doped Carbon Coated with CoP for Efficient Hydrogen Evolution. *ACS Catal.* **2017**, *7* (6), 3824–3831. https://doi.org/10.1021/acscatal.7b00587.

(44) Yasuda, S.; Yu, L.; Kim, J.; Murakoshi, K. Selective Nitrogen Doping in Graphene for Oxygen Reduction Reactions. *Chem. Commun.* **2013**, *49* (83), 9627–9629. https://doi.org/10.1039/c3cc45641b.

(45) Lai, L.; Potts, J. R.; Zhan, D.; Wang, L.; Poh, C. K.; Tang, C.; Gong, H.; Shen, Z.; Lin, J.; Ruoff, R. S. Exploration of the Active Center Structure of Nitrogen-Doped Graphene-Based Catalysts for Oxygen Reduction Reaction. *Energy Environ. Sci.* **2012**, *5* (7), 7936–7942. https://doi.org/10.1039/c2ee21802j.

(46) Wang, L.; Guo, X.; Chen, Y.; Ai, S.; Ding, H. Cobalt-Doped g-C 3 N 4 as a Heterogeneous Catalyst for Photo-Assisted Activation of Peroxymonosulfate for the Degradation of Organic Contaminants. *Appl. Surf. Sci.* **2019**, *467–468* (August 2018), 954–962. https://doi.org/10.1016/j.apsusc.2018.10.262.

(47) Song, Q.; Li, J.; Wang, L.; Pang, L.; Liu, H. Controlling the Chemical Bonding of Highly Dispersed Co Atoms Anchored on an Ultrathin G-C3N4@Carbon Sphere for Enhanced Electrocatalytic Activity of the Oxygen Evolution Reaction. *Inorg. Chem.* **2019**, *58* (16), 10802–10811. https://doi.org/https://pubs.acs.org/doi/10.1021/acs.inorgchem.9b01089.

(48) Xie, M.; Tang, J.; Kong, L.; Lu, W.; Natarajan, V.; Zhu, F.; Zhan, J. Cobalt Doped G-C 3 N 4 Activation of Peroxymonosulfate for Monochlorophenols Degradation. *Chem. Eng. J.* **2019**, *360* (September 2018), 1213–1222. https://doi.org/10.1016/j.cej.2018.10.130.

(49) Ma, T. Y.; Dai, S.; Jaroniec, M.; Qiao, S. Z. Metal-Organic Framework Derived Hybrid Co3O4-Carbon Porous Nanowire Arrays as Reversible Oxygen Evolution Electrodes. *J. Am. Chem. Soc.* **2014**, *136* (39), 13925–13931. https://doi.org/10.1021/ja5082553.